

# Charge exchange and electron emission in slow collisions of highly charged ions with C<sub>60</sub>

Uwe Thumm

Department of Physics, Kansas State University, Manhattan, KS 66506-2601, USA

Received 23 February 1994, in final form 3 May 1994

**Abstract.** We simulated the population dynamics of target and projectile levels during the interaction of slow, highly charged ions and C<sub>60</sub>. Our investigation is based on a semiclassical over-barrier description of long-range charge exchange and a spherical model for the C<sub>60</sub> cluster. It includes the transient formation of hollow atoms and relaxation of the projectile due to Auger cascades. As a first application, we consider slow Ar<sup>3+</sup> projectiles and give estimates for the occupation changes of all coupled target and projectile levels, charge-state evolutions and energy-resolved spectra of emitted Auger electrons. Our results are in satisfactory agreement with recent experimental data.

## 1. Introduction

The possibility of making large hollow carbon cages was pointed out in 1966 (Jones 1966), and the existence of C<sub>60</sub> (buckyball or buckminsterfullerene) was first suggested in 1970 (Osawa 1970, 1971). In experiments done in 1985 by Kroto *et al* (1985), C<sub>60</sub> was discovered to be stable and in 1990 C<sub>60</sub> was made available in substantial quantities (Krätschmer *et al* 1990).

Information on the electronic structure and collective excitation modes of C<sub>60</sub> has been obtained from various optical absorption and photoionization measurements using solutions, solids, gases and supersonic beams of C<sub>60</sub>, and from electron-impact energy-loss experiments on solid and gaseous C<sub>60</sub>. An extensive review of C<sub>60</sub> research has been published by Kroto *et al* (1991) and an update of the experimental research can be found in the introduction of the paper by Wang *et al* (1993).

Very recently, experiments have been carried out by Walch *et al* (1994) that probed the interaction between slow highly charged ions (80 keV Ar<sup>3+</sup>, 140 keV Xe<sup>14+</sup>) and gaseous C<sub>60</sub> targets. They measured the charge-state distribution of the target after the collision in coincidence with the final projectile charge state and absolute cross sections for the production of specific target charge states.

Theoretically, the electronic structure of the C<sub>60</sub> cluster is well understood from first-principles calculations (Satpathy 1986, Saito and Oshiyama 1991, Weaver *et al* 1991). Predictions based on such calculations are in good agreement with photoemission and inverse-photoemission measurements (Weaver *et al* 1991, Benning *et al* 1991, Jost *et al* 1991). The decomposition of *ab initio* wavefunctions in a spherical basis shows that almost all wavefunctions of the valence band and the bottom of the conduction band of C<sub>60</sub> can be characterized by angular-momentum eigenstates. According to this decomposition, Martins *et al* (1991) suggested that the electronic structure of C<sub>60</sub> could be modelled as a spherical shell of radius  $a = 6.7 a_0$  and width  $\Delta a = 5.6 a_0$  (approximately twice the atomic radius of carbon,  $a_0$  is the atomic unit of length) by using an attractive effective potential.

Such a spherical-shell model for  $C_{60}$  was further developed by Puska and Nieminen (1993). Their model, which we shall adopt for our simulation, is based on a simplified description of the positive charge distribution inside the spherical shell within the jellium approximation (which assumes a smeared out positive-charge background) and includes a correction beyond the jellium model. This correction adds the effects of the ionic cores by using an additional effective square potential of depth  $w_0$  inside the shell. The model includes two adjustable parameters, the positive background charge density of the standard jellium model  $n_0$  and  $w_0$  which are chosen as  $r_s = (4/3\pi n_0)^{-1/3} = 1.2 a_0$  and  $w_0 = 19$  eV. The density parameter  $r_s$  lies somewhat below the range  $2 a_0 < r_s < 6 a_0$  of most metals. It is worth mentioning that this value for  $r_s$  is almost reproduced for a spherical shell that contains the uniformly smeared out charge of 240 valence electrons; with the values for  $a$  and  $\Delta a$  from above, we obtain an electron density  $\tilde{n}_0 = 7.2 a_0^{-3}$  and  $\tilde{r}_s = 1.5 a_0$ . With the given values for  $a$ ,  $\Delta a$ ,  $r_s$  and  $w_0$ , Puska and Nieminen used the local density approximation in order to self-consistently determine an effective one-electron potential and its spectrum of valence-electron states together with the occupations and degeneracies of these states.

Inspired by the experiments of Walch *et al* (1994) and a theoretical and experimental study of the neutralization dynamics of highly charged ions approaching a metal surface by Burgdörfer *et al* (1991), we developed a classical simulation for the dynamical interaction of slow highly charged ions with spherical clusters. This paper is organized as follows. In section 2, we describe the electronic structure of target and projectile. Section 3 specifies interaction potentials and the potential barrier between projectile and target. In section 4, we outline our simulation of the evolution of level occupations, energy levels and charge states of target and projectile, the projectile motion, and the emission of Auger electrons during the collision. The basic input for this dynamical study is provided in section 5 where we obtain electronic transition rates within a classical over-barrier model. In section 6, we show first numerical results. A summary and our conclusions are contained in section 7. Atomic units are used unless otherwise stated.

## 2. Electronic structure of target and projectile

### 2.1. Target

We describe the electronic structure of  $C_{60}$  on the basis of the energy levels, degeneracies and occupations calculated by Puska and Nieminen (1993) within a one-electron spherical-shell model. With respect to target level  $m$ , we denote the unperturbed energy by  $\epsilon_m^{(t,0)}$ , the perturbed energy by  $\epsilon_m^{(t)}(R)$ , the initial occupation by  $b_m^0$ , the instantaneous occupation by  $b_m(R)$  and the degeneracy by  $B_m$ .  $R$  is the distance between the target centre-of-mass and the projectile. We assume that the 240 valence electrons occupy the lowest energy levels in table 1 ranging from the bottom of the valence band at  $\epsilon_1^{(t,0)} = V_0 = -33.7$  eV to the highest occupied level, the Fermi level, at  $\epsilon_{15}^{(t,0)} = -7.44$  eV. The remaining 120 electrons of  $C_{60}$  occupy core levels localized near individual carbon nuclei and are of no direct interest to us. The spherical model gives level degeneracies equal to  $2(2l + 1)$  such that all levels below  $\epsilon_{15}^{(t,0)}$  are fully occupied. Level  $m = 15$  is partially occupied with  $b_{15}^0 = 28$  electrons and levels above  $\epsilon_{15}^{(t,0)}$  are empty.

During the interaction with a highly charged ion, the target spectrum is Stark shifted towards lower energies in the electric field of the projectile. After the capture or emission of target electrons, positive charge accumulates on the target which results in an additional downward shift of the target levels. The latter effect provides a simple quantitative

**Table 1.** Electronic structure of C<sub>60</sub> according to Puska and Nieminen (1993, 1994). Energy  $\epsilon_m^{(t,0)}$  in eV, angular momentum  $l$ , level degeneracy  $B_m = 2(2l + 1)$  and ground-state occupation  $b_m^0$  of level  $m$

$m$	$l$	$ \epsilon_m^{(t,0)} $	$B_m$	$b_m^0$
20	1	0.66	6	0
19	0	1.36	2	0
18	10	2.18	42	0
17	6	2.27	26	0
16	5	6.04	22	0
15	9	7.44	38	28
14	4	9.31	18	18
13	3	12.01	14	14
12	8	12.33	34	34
11	2	14.10	10	10
10	1	15.52	6	6
9	0	16.25	2	2
8	7	16.80	30	30
7	6	20.83	26	26
6	5	24.37	22	22
5	4	27.40	18	18
4	3	29.88	14	14
3	2	31.78	10	10
2	1	33.06	6	6
1	0	33.70	2	2

explanation for the increase in ionization energy for the sequential removal of target electrons (Smith 1961): the work for removing  $k$  target electrons from a spherical conductor of radius  $a$  is  $W_k = k\Phi + k^2/2C$  where  $\Phi$  is the workfunction and  $C = a$  the capacitance. Accordingly, the  $k$ th ionization energy is

$$I_k = W_k - W_{k-1} = I_1 + (k - 1)/a \tag{1}$$

with the first ionization energy  $I_1 = \Phi + (2a)^{-1} = -\epsilon_{15}^{(t,0)}$ . The additional shift corresponds to the energy required to move an electron from just above the surface of the shell to infinity and amounts to  $a^{-1} \approx 4$  eV. Due to the high degeneracy of the highest occupied state ( $m = 15$ ), all ionization potentials  $I_k$  with  $k \leq b_{15}^0$  can be derived from the unperturbed energy  $\epsilon_{j5}^{(t,0)}$  by using (1). Physically, the restriction  $k \leq b_{15}^0$  is irrelevant in view of strong experimental evidence that C<sub>60</sub> fragments after the removal of not more than seven electrons (Walch *et al* 1994).

The total charge of the target is obtained from the set  $\{b_m(R)\}$  of occupation numbers

$$q^{(t)}(R) = \sum_m \{b_m^0 - b_m(R)\} = 240 - \sum_m b_m(R) \tag{2}$$

and the energy of the shifted target levels is given by

$$\epsilon_m^{(t)}(R) = \epsilon_m^{(t,0)} - q^{(p)}(R)/R - q^{(t)}(R)/a.$$

### 2.2. Projectile

We assume hydrogenic projectile levels and denote energy levels, occupation numbers and degeneracies by  $\epsilon_n^{(p)}(R)$ ,  $a_n(R)$  and  $A_n = 2n^2$ . We refer to initial unperturbed electronic energies and occupations by  $\epsilon_n^{(p,0)}$  and  $a_n^0$  and to the initial charge by  $q^{(p,0)}$ .

During the interaction with the target, the energetic positions of the projectile levels change due to image charge effects, Stark shifts and the dynamical change in inner and outer screening induced by varying populations. Level shifts provoked by induced image charges of projectile electrons and nucleus are discussed in more detail below. For highly charged ions incident on metallic clusters, these energy shifts are positive due to an overwhelming negative image charge of the projectile nucleus. As soon as the charge-exchange process starts (at some critical distance to be specified below), the target becomes charged and Stark shifts strongly dominate image shifts.

A projectile with nuclear charge  $q_{\text{nuc}}$  and occupation numbers  $\{a_n(R)\}$  has the total charge

$$q^{(p)}(R) = q_{\text{nuc}} - \sum_n a_n(R). \quad (3)$$

Including the possibility for inner and outer screening, the effective charge for a projectile level of principal quantum number  $n$  is

$$Z_n^{(p)}(R) = q_{\text{nuc}} - \sum_{n'} S_{n,n'} a_{n'}(R) \quad (4)$$

with the matrix of screening parameters  $S$ . The energy of the shifted projectile levels, including image shift  $V_{\text{im}}$  and Stark shift, is

$$\epsilon_n^{(p)}(R) = -\frac{Z_n^{(p)}(R)}{2n^2} + V_{\text{im}}(R) - q^{(t)}(R)/R.$$

### 3. Interaction potentials and saddle geometry

On its way towards the initially neutral target, the projectile first experiences the dynamical response of the target electron gas. This collective response of mainly conduction electrons of the target constitutes a many-body problem that can be represented by the time-dependent superposition of collective excitation modes, plasmons, of the target. At sufficiently large distances  $R$ , and for small projectile velocities, the collective response is well represented by a velocity-independent classical image potential.

In what follows, we choose the  $z$ -axis of the target-centred coordinate system along  $\mathbf{R}$  such that the projectile nucleus is located at  $\mathbf{R} = (0, 0, R)$ . We denote position vectors of the active electron in the target frame of reference by  $\mathbf{x}$  and in the projectile frame by  $\mathbf{x}' = \mathbf{x} - \mathbf{R}$ .

The LDA calculation of Puska and Nieminen (1993) yields a static polarizability of the  $\text{C}_{60}$  cluster of  $\alpha = 618$  which can be related to the classical result for a conducting sphere of radius  $\tilde{a}$  by  $\tilde{a} = \sqrt[3]{\alpha} = 8.52$ . Therefore, with respect to image potentials, we use the radius  $\tilde{a}$  instead of  $a$ . The classical image potential at a location  $\mathbf{x}$ , due to the image field generated by a charge  $q$  at a location  $\mathbf{R}$  that interacts with a conducting sphere, is (Jackson 1975)

$$V_{\text{im}}^{(q)} = -\frac{\tilde{a}q}{R} \left\{ \left| \mathbf{x} - \frac{\tilde{a}^2}{R^2} \mathbf{R} \right|^{-1} - |\mathbf{x}|^{-1} \right\}$$

where the coordinate origin coincides with the centre of the sphere.

During charge exchange, the active electron is affected by both the image potential of the projectile of charge  $q$  and by its self-image potential

$$V_{\text{im}}^{(e)} = \frac{\tilde{a}}{x^2} \left\{ \left| 1 - \frac{\tilde{a}^2}{x^2} \right|^{-1} - 1 \right\}$$

leading to the total image potential

$$V_{\text{im}} = V_{\text{im}}^{(q)} + V_{\text{im}}^{(e)}$$

which, for large  $R$ , behaves as

$$V_{\text{im}} = \frac{\tilde{a}}{R^4} \left\{ \tilde{a}^2(1 - q) + \frac{1}{2}qz^2 \right\} + O(R^{-5}).$$

The asymptotic  $R^{-4}$  behaviour of the leading term reflects the dominant induced-dipole character of the image potential at large projectile–target distances  $R$ . The rapid decrease in  $R$  explains the above-mentioned irrelevance of the image potential for charged targets.

Within the over-barrier model, we assume that the active electron moves along the  $z$ -axis. Along this axis the total image potential can be written as

$$V_{\text{im}}(q, R, z) = -\frac{\tilde{a}q}{R} \left\{ \left| z - \frac{\tilde{a}^2}{R} \right|^{-1} - z^{-1} \right\} + \frac{\tilde{a}}{z} \left\{ \left| z - \frac{\tilde{a}^2}{z} \right|^{-1} - z^{-1} \right\}$$

where the  $q$ -independent term represents the electronic self-image potential. The total potential that acts on an active electron during charge transfer is

$$V(q, Q, R, z) = \frac{q}{|R - z|} + \frac{Q}{z} + V_{\text{im}}(q, R, z) \tag{5}$$

where  $q$  and  $Q$  are the total charges of projectile and target acting on the electron in transition. For electrons leaving the target  $q = q^{(p)}(R)$  and  $Q = q^{(t)}(R) + 1$  where  $q^{(p)}(R)$  and  $q^{(t)}(R)$  are the charges immediately before the active electron left the target. Similarly, if the active electron originates in the projectile, we use  $q = q^{(p)}(R) + 1$  and  $Q = q^{(t)}(R)$ .

According to the classical over-barrier model, the active electron has to overcome the potential well between projectile and target in order to be captured by the projectile or recaptured by the target. The location and height of the potential barrier is determined by the total potential (5) acting on the active electron. We designate the location of the saddle, i.e. the location of the maximum of  $V(q, Q, R, z)$ , by  $z_B(q, Q, R)$ . The height of the potential barrier is then given by  $V_B(q, Q, R) = V(q, Q, R, z_B)$ . In our numerical applications, we found that  $z_B$  changes very little if we omit the image potentials. Without image potentials, and for a target of point charge  $Q \neq 0$ , the location of the maximum of  $V(q, Q, R, z)$  and the barrier height can be approximated analytically as

$$\tilde{z}_B(q, Q, R) \approx R \left( 1 + \sqrt{q/Q} \right) \tag{6}$$

and

$$V_B(q, Q, R) \approx -R^{-1} \left( Q + q + 2\sqrt{qQ} \right). \tag{7}$$

Application of the over-barrier model to long-range charge exchange between highly charged ions and  $C_{60}$  requires modifications of the above expressions for  $z_B$  and  $V_B$ . Clearly,  $z_B$  is limited to the spatial interval between the target surface located at  $a + \Delta a/2$  and  $R$ . In order to include the case  $Q = 0$ , for which (6) does not apply, we determine the saddle location according to

$$z_B(q, Q, R) = \begin{cases} \max\{\tilde{z}_B(q, Q, R), a + \Delta a/2\} & \text{if } Q \neq 0 \\ a + \Delta a/2 & \text{if } Q = 0. \end{cases}$$

Let us now consider an electron with enough energy  $\epsilon \geq V_B$  to cross the potential barrier. The size of the classically-allowed transition region at  $z = z_B$  strongly depends on the energy difference  $\epsilon - V_B$  and is monotonically increasing in this excess energy. The width  $x_B$  of this region along a direction (here taken as the  $x$ -axis) perpendicular to the  $z$ -axis can be easily calculated numerically from the total potential (5). At this point, the simplifying assumption of the electron moving along the  $z$ -axis has to be dropped and, instead of the total potential (5) valid for electron positions  $x = (0, 0, z)$ , the corresponding  $x = (x, 0, z)$ -dependent expression has to be used, leading to the condition for  $x_B$

$$V_B(q, Q, R, z_B, x_B) = \epsilon.$$

Finally, the geometrical cross section of the saddle for the electron in transition is

$$\sigma_B(q, Q, R, \epsilon) = \begin{cases} \pi x_B^2 & \text{if } \epsilon > V_B \\ 0 & \text{otherwise.} \end{cases} \quad (8)$$

#### 4. Dynamics

In this section, we discuss the classical rate equations that determine the time evolution of occupation numbers for projectile and target levels. These equations will be integrated numerically together with Newton's equations for the motion of the centre-of-mass of the scattering system and the rate equations for the emission of Auger electrons into specified energy bins.

##### 4.1. Projectile motion

At large projectile-target distances  $R$  and long before charge exchange becomes possible, the projectile is merely slightly repelled by the image potential it induces in the target. As  $R$  decreases below a critical value for the onset of electron capture  $R_1^*$ , the projectile motion becomes predominantly determined by the Coulomb interaction between both, now charged, collision partners and continues to move on a dynamic Coulomb trajectory.

For a projectile incident with impact parameter  $b$  and velocity  $v_0$  along the  $z$ -axis, the initial conditions (at time  $t_0$ ) for its position and velocity are

$$R(t_0) = b + v_0 t_0 \quad v(t_0) = v_0.$$

Integration of Newton's equation,

$$\frac{d}{dt}v = \mu^{-1}F$$

with the reduced mass  $\mu$  of the target and projectile and the force

$$F(R) = \nabla \left\{ \frac{q^{(t)}(R)q^{(p)}(R)}{R} + W_{\text{im}}^{(q^{(p)})}(R) \right\}$$

yields  $R(t)$  and  $v(t)$  at any time  $t$ . The self-image potential energy of the projectile of charge  $q^{(p)}(R)$  (cf section 3) is

$$W_{\text{im}}^{(q^{(p)})} = -\frac{\tilde{a}^3 q^{(p)}(R)^2}{R^2(R^2 - \tilde{a}^2)}.$$

#### 4.2. Occupation dynamics of projectile and target levels

In our semiclassical model, we picture resonant charge exchange as the classical motion of one active electron from an initial quantum state to a final quantum state. Electronic transitions are further assumed to be so fast that  $R$  practically does not change during the transition time (adiabatic approximation).

In order to use quantum and classical concepts at the same time, we need to subdivide the classical electronic energy continuum into energy bins. Thus, in formulating the condition for resonant charge exchange between projectile level  $n$  and target level  $m$ , we require that a shifted target level of energy  $\epsilon_m^{(t)}(R)$  lies within the energy bin  $[\epsilon_n^{(p)}(R)]$  associated with the shifted projectile level  $n$  of energy  $\epsilon_n^{(t)}(R)$

$$\begin{aligned} \epsilon_m^{(t)}(R) &\in [\epsilon_n^{(p)}(R)] \\ &\equiv [\frac{1}{2}(\epsilon_n^{(p)}(R) - \epsilon_{n-1}^{(p)}(R)), \frac{1}{2}(\epsilon_{n+1}^{(p)}(R) - \epsilon_n^{(p)}(R))]. \end{aligned} \tag{9}$$

As the projectile approaches the target, the first resonant transfer of an electron becomes possible when the potential barrier  $V_B$  energetically moves below the highest occupied target level,  $\epsilon_{15}^{(t)}(R)$ . The distance  $R_1^*$  at which this may happen is obtained numerically from the (necessary) condition

$$\epsilon_{15}^{(t)}(R_1^*) = V_B(q, Q, R_1^*)$$

where  $q = q^{(p,0)}$  and  $Q = 1$ . The generalization of this condition leads to decreasing critical radii  $R_1^* > R_2^* > R_3^* \dots$  for the sequential capture of electrons on the incoming trajectory. An approximate expression for  $R_1^*$ , obtained analytically by using (7), is

$$R_1^* \approx \frac{1 + 2\sqrt{q^{(p,0)}}}{|\epsilon_{15}^{(t,0)}|}. \tag{10}$$

For the known initial occupations of target and projectile,  $a_n^0$  and  $b_m^0$ , we obtain the occupation numbers at any time  $t > t_0$  by integrating the rate equations (for convenience we omit the variable  $t$ )

$$\begin{aligned} \frac{d}{dt} a_n &= \Gamma_{\text{RN}} \Theta(A_n - a_n) - \Gamma_{\text{RL}} a_n + w_{f,n} \sum_{n' > n} \Gamma_{n',n} w_{i,n'} - 2\omega_{i,n} \sum_{n' < n} \Gamma_{n,n'} \omega_{f,n'} \\ \frac{d}{dt} b_m &= -\Gamma_{\text{RN}} \Theta(A_n - a_n) + \Gamma_{\text{RL}}. \end{aligned} \tag{11}$$

All rates  $\Gamma$  and occupation numbers implicitly depend on  $R(t)$  and the above equations have to be solved simultaneously with Newton's equation for the projectile motion (cf previous section). Expressions for the resonant neutralization rate ( $\Gamma_{\text{RN}}$ ), resonant loss rate ( $\Gamma_{\text{RL}}$ ) and projectile Auger ionization rate ( $\Gamma_{n,n'}$ ) are given in section 5.  $\Theta$  is the unit step function, i.e.  $\Theta = 0$  for  $x \leq 0$  and  $\Theta = 1$  for  $x > 0$ . With the factor  $\Theta(A_n - a_n)$ , we allow resonant neutralization only if the final state is not fully occupied.

We only consider fast Auger transitions for which the two active electrons are initially in the same state  $n$ . We further assume that the total number of Auger transitions is proportional to the number of possible combinations of two electrons in the initial shell. The statistical weight for the initial state of an Auger transition is then given by

$$w_{i,n} = \frac{1}{2}(a_n^2 - a_n)\Theta(a_n - 2).$$

With respect to the number of accessible final states, a reasonable statistical weight would be

$$w_{f,n} = (A_n - a_n)\Theta(A_n - a_n)$$

which puts equal weight on all final states in shell  $n$ . In conjunction with the transition rates specified in section 5.3, Burgdörfer *et al* (1991) proposed the empirical-weight function

$$w_{f,n} = (1 - 1.5a_n)^{-1}$$

which we shall adopt and which, as our previous expression, contains the same basic and qualitatively correct physical assumption that the Auger terms in (11) are monotonically (not necessarily linearly) increasing in the number of vacant bound final states.

### 4.3. Auger electron emission

The energy of an Auger electron emitted at time  $t$  from level  $n_i$  while a second projectile electron transfers from  $n_i$  to a lower level  $n_f$  is, within our independent electron picture, given by

$$\epsilon_A(t) = 2\epsilon_{n_i}^{(p)}(R(t)) - \epsilon_{n_f}^{(p)}(R(t)).$$

By collecting the emitted Auger electrons in energy bins  $[\epsilon_k] \equiv [(k-1)\Delta\epsilon, k\Delta\epsilon]$ ,  $k = 1, 2, \dots$ , we obtain a rate equation for the number  $c_k(t)$  of electrons emitted in each energy bin before time  $t$

$$\frac{d}{dt}c_k = \sum_{n_f} w_{f,n_f} \sum_{n_i > n_f} \Gamma_{n_i,n_f} w_{i,n_i} \begin{cases} 1 & \text{if } \epsilon_A(t) \in [\epsilon_k] \\ 0 & \text{otherwise.} \end{cases}$$

$\Delta\epsilon$  is of the order of the experimental energy resolution.

## 5. Transition rates

We now derive expressions for the electronic transition rates. The rates for resonant capture and loss are obtained within a one-electron picture of the electron-transfer process.

5.1. Resonant capture

In analogy to a free electron gas, a valence electron with energy  $\epsilon_m^{(t,0)}$  can be assigned the velocity  $\tilde{v}_m$  given by  $\tilde{v}_m^2 = 2(\epsilon_m^{(t,0)} - \epsilon_1^{(t,0)})$ . The interaction with the projectile ion leads to the Stark shift of target levels and the formation of a potential barrier  $V_B(q, Q, R)$ . If the valence electron is energetic enough to overcome the potential barrier, its velocity  $v_m$ , by the time it has reached the saddle, is

$$v_m(R)^2 = 2(\epsilon_m^{(t)}(R) - V_B(q, Q, R)).$$

We assume that electrons are transferred along the axis joining the centres of mass of projectile and target. Taking energy dissipation along the directions perpendicular to this 'internuclear axis' into account, the velocity component relevant for capture is reduced to  $\bar{v}_m = \sqrt{2/3}v_m$ . The average density of target electrons in level  $m$  confined inside the spherical shell of volume  $V$  is

$$\rho_m(R) = \frac{b_m(R)}{V} \quad V = \frac{4}{3}\pi(3a^2\Delta a + \frac{1}{4}\Delta a^3).$$

The current density for resonant over-barrier capture from a Stark-shifted target level  $m$  into the energy bin  $[\epsilon_n^{(p)}(R)]$  of the projectile now follows as

$$j_n(R) = \begin{cases} \sqrt{\frac{2}{3}}\rho_m(R)v_m(R) & \text{if } \epsilon_m^{(t)}(R) \in [\epsilon_n^{(p)}(R)] \\ 0 & \text{otherwise.} \end{cases}$$

Finally, the current of resonantly captured target electrons, i.e. the instantaneous rate for resonant capture, is obtained as the product of current density and geometrical cross section (8)

$$\Gamma_{RN}(R) = \sum_{\epsilon_m^{(t)}(R) \in [\epsilon_n^{(p)}(R)]} j_n(R)\sigma_B(q^{(p)}(R), Q, R, \epsilon_m^{(t)}(R))$$

where  $Q = q^{(p)}(R) + 1$  and the sum extends over all target levels that are in resonance with the  $n$ th projectile-energy bin.

5.2. Resonant loss

Resonant loss is the transfer of a projectile electron bound with energy  $\epsilon_n^{(p)}(R)$  into a vacant target level of energy  $\epsilon_m^{(t)}(R) \in [\epsilon_n^{(p)}(R)]$ . Projectile electrons in level  $n$  approach the surface at a rate that is approximately given by the classical frequency of revolution in a Coulomb orbit

$$v_n(R) = \frac{Z_n^{(p)}(R)^2}{2\pi n^3}.$$

The radial expectation value for these electrons, averaged over all orbital angular momenta, is

$$\langle r_n \rangle = \frac{5n^2 + 1}{4Z_n^{(p)}(R)}.$$

We assume that resonant loss occurs only if the active electron reaches the saddle located at  $z_B$ , i.e. if  $0 \leq R - z_B \leq \langle r_n \rangle$ . For an electron confined in a sphere of radius  $\langle r_n \rangle$ , the overlap of this sphere with a plane through  $z_B$  and perpendicular to the 'internuclear axis' defines a circle of radius

$$x_n(R) = \sqrt{\langle r_n \rangle^2 - (R - z_B)^2}$$

and area  $\sigma_n = \pi x_n(R)^2$ . The active electron hits the saddle with a probability that can be estimated as

$$p(R, \epsilon_n^{(p)}(R)) = \begin{cases} 1 & \text{if } \sigma_B > \sigma_n \\ \sigma_B / \sigma_n & \text{if } \sigma_B \leq \sigma_n \end{cases}$$

such that the rate for resonant loss out of projectile level  $n$  is

$$\Gamma_{RL}(R) = \nu_n(R) p(R, \epsilon_n^{(p)}(R)) \sum_{\epsilon_m^{(q)}(R) \in \{\epsilon_n^{(p)}(R)\}} \Theta(\epsilon_m^{(q)}(R) - V_B(q, Q, R)) \Theta(B_m - b_m(R)).$$

The sum includes all target levels that are in resonance with the  $n$ th projectile-energy bin, not fully occupied and energetically above the classical barrier.

### 5.3. Auger transitions

In modelling the relaxation of projectiles in multiple excited states, we follow the work of Burgdörfer *et al* (1991) where an estimate for the fastest Auger transitions, with two equivalent active electrons in the initial state, was obtained by fitting various  $1sn_i s^2 \rightarrow 1sn_f \epsilon s$  rates calculated from the 'Cowan code' (Cowan 1981). This fit leads to

$$\Gamma_{n_i, n_f} = \frac{5.06 \times 10^{-3}}{(n_i - n_f)^{3.46}}$$

and is improved by a correction factor, approximately equal to 0.5, chosen to include configurations of non-equivalent active electrons in the initial state.

## 6. Numerical results for $\text{Ar}^{8+}$ on $\text{C}_{60}$

For the numerical propagation of the coupled rate equations of section 4, we increased the number of mesh points until convergence was obtained. In order to control the numerical precision, we made sure that the total charge remained unchanged. With  $N_A(t)$  being the total number of Auger electrons emitted before time  $t$ , charge conservation is guaranteed if, after every time step,

$$q^{(p)}(t) + q^{(t)}(t) - N_A(t) = q^{(p,0)}$$

holds.

We determined the screening matrix  $S$  in (4) by assuming full screening by inner and no screening by outer electrons, i.e.  $S_{n,n'} = 1$  for  $n' < n$  and  $S_{n,n'} = 0$  for  $n' \geq n$ .

### 6.1. Evolution of charge states, occupations and electron emission

In order to study the evolution of charge states, occupation numbers and the emission of Auger electrons during the collision, we considered projectile trajectories with impact parameter  $b = 15$ . As projectile velocity, we chose  $v = 0.28$  corresponding to 80 keV  $Ar^{8+}$  ions used in the recent experiment by Walch *et al* (1994). Figure 1 shows the evolution of projectile and target charge states during the collision, together with the number of emitted projectile Auger electrons. The distance  $R_{\parallel}$  on the abscissa is the projection of the projectile–target distance  $R$  on the direction of the incoming projectile. Thus, for the incoming trajectory  $R_{\parallel} < 0$ , for the outgoing trajectory  $R_{\parallel} > 0$  and  $R_{\parallel} = 0$  at the point of closest approach. As the projectile approaches the  $C_{60}$  cluster, charge exchange starts at the critical distance  $R_{\parallel} = (R_1^{*2} - b^2)^{1/2} \approx 21$  ( $R_1^* \approx 26$ ). Subsequently, the projectile captures additional electrons and reaches its lowest charge state near the point of closest approach on the outgoing trajectory. Shortly thereafter, resonant charge exchange stops and the target charge remains unchanged while the projectile charge increases due to Auger relaxation. The results discussed in this subsection are for  $R_{\parallel} < 150$ . At larger distances  $R_{\parallel}$ , i.e. further down-stream, the projectile continues to relax by emitting Auger electrons.

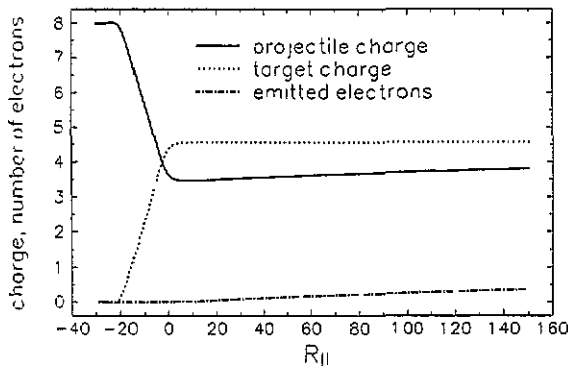


**Figure 1.** Charge-state evolution and Auger emission for 80 keV (corresponding to a speed  $v = 0.28$ )  $Ar^{8+}$  ions colliding with  $C_{60}$  with impact parameter  $b = 15$ . The distance  $R_{\parallel}$  is the projection of the target–projectile distance onto the incident-beam direction; at the point of closest approach  $R_{\parallel} = 0$ .

A more detailed picture of the neutralization dynamics is given in figure 2 where changes in occupation numbers (i.e. the instantaneous occupation minus the initial occupation of a particular level) are shown as a function of  $R_{\parallel}$  and for those projectile levels  $n$  (figure 2(a)) and target levels  $m$  (figure 2(b)) that are coupled. With respect to the target (figure 2(b)), the highest occupied level  $m = 15$  participates by far the most actively in the charge-exchange process and loses several electrons to the incoming projectile. Note that some resonant loss to the highest target levels occurs. For the projectile (figure 2(a)), levels  $n = 6$  and 7 get resonantly fed by target level  $m = 15$  on the incoming trajectory. Auger relaxation of the projectile on the outgoing trajectory leads to the depletion of projectile levels  $n = 6$  and 7 and increases the population in projectile levels  $n = 3$  and 4. In the shown  $R_{\parallel}$  interval this depletion is not completed and the projectile keeps electrons in highly-excited states. It therefore continues to relax by emitting electrons as it moves further away from the target.

Occupation changes induced by resonant processes can also be understood by looking at the strongly-coupled energy levels and the potential barrier as a function of  $R_{\parallel}$ . As shown

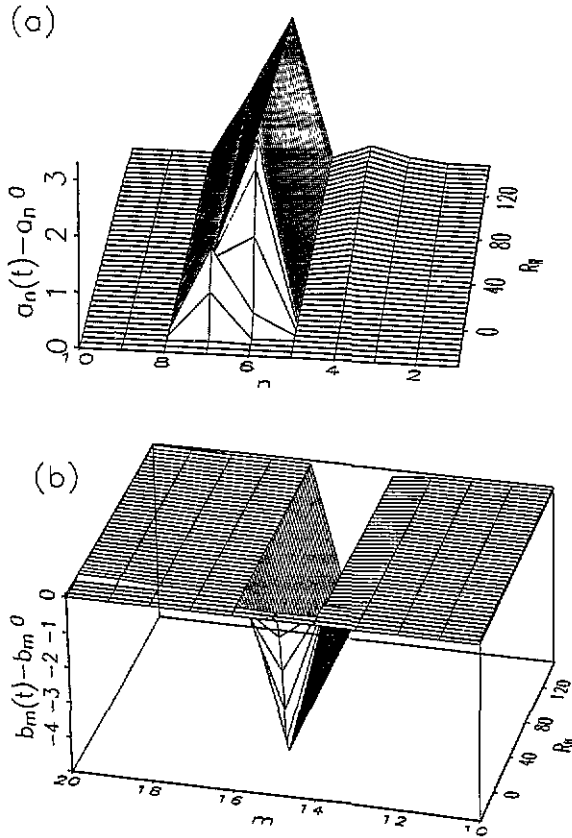


**Figure 2.** Evolution of the changes of projectile (a) and target (b) occupation numbers during the collision. Collision system and parameters as in figure 1. Projectile states are labelled by  $n$ , target states by  $m$ .

in figure 3, projectile level  $n = 6$  crosses target level  $m = 15$ . The crossing occurs above the potential barrier for capture and near the point of closest approach. This results in a large current of target electrons from level  $m = 15$  that are classically allowed to transfer to projectile level  $n = 6$ .

The time-dependent emission of Auger electrons is shown in figure 4 where the Auger yield, differential in energy, is plotted against  $R_{\parallel}$  and the energy of the emitted electron. The emitted electrons are collected in energy bins of width 4.4 eV. Note that the displayed electron yield is normalized to a single projectile. Auger electrons are emitted in two spectral regions, one extending from threshold to about 10 eV due to Auger transitions that populate level  $n = 4$  and one in the range between about 40–50 eV corresponding to transitions into  $n = 3$ . Within each structure, the slowest electrons are emitted first and the most energetic electrons are emitted at larger distances from the target.

In order to address the sensitivity of the charge states on the resonant transition rate  $\Gamma_{RN}$ , we multiplied  $\Gamma_{RN}$  by a constant adjustable factor  $c_{RN}$ . Table 2 shows the charge of the target  $q^{(t)}(R_{\parallel} = 150) = q^{(t)}(\infty)$  after we replaced  $\Gamma_{RN}$  by  $c_{RN}\Gamma_{RN}$ . Surprisingly,  $q^{(t)}(\infty)$  is relatively weakly sensitive to changes in  $c_{RN}$  and depends weakly on the exact magnitude of  $\Gamma_{RN}$ .

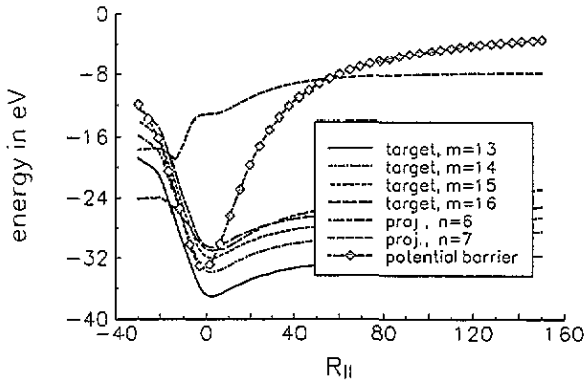


Figure 3. Energy levels of target states  $m = 13 \dots 16$  and projectile states  $n = 6$  and  $7$ , together with the barrier for classical over-barrier capture. Collision system and parameters as in figures 1 and 2.

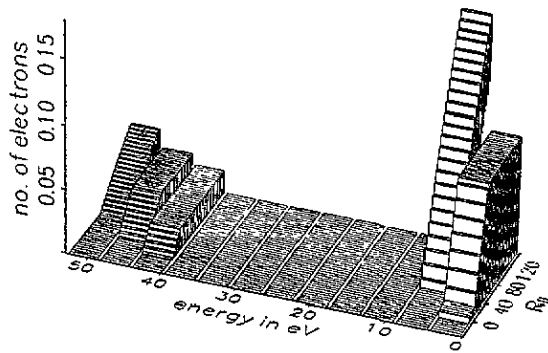


Figure 4. Emission of projectile Auger electrons during the collision into energy bins of width 4.4 eV. Collision system and parameters as in the previous figures.

Table 2. Scaling factor  $c_{RN}$  for  $\Gamma_{RN}$  and final charge state of the target for 80 keV Ar<sup>B+</sup> on C<sub>60</sub> with  $b = 15$ .

$c_{RN}$	0.1	0.5	1.0	1.5	5.0
$q^{(0)}(\infty)$	3.71	4.47	4.61	4.66	4.72

6.2. Impact-parameter dependence of charge states, occupation numbers and Auger spectra

In figure 5, we show the final charge states of projectile and target, together with the number of emitted Auger electrons. The results shown are calculated for integer impact parameters  $b$  and are spline interpolated. All results in this subsection include the downstream Auger relaxation for  $R_{||} > 150$  mentioned in the previous section. Note, however, that complete Auger relaxation is included only with respect to the fastest Auger transitions discussed in section 5.3. Within our classical model no electronic interaction is possible if the projectile trajectory does not intersect with a sphere of radius  $R_1^*$  around the target. Therefore no charge exchange occurs for impact parameters larger than about 26. According to our simulation, Auger electrons are emitted for not too distant collisions ( $b < 18$ ). For

more distant collisions ( $18 < b < R^*$ ) resonant charge exchange still occurs; however, no emission of Auger electrons is predicted (in fast Auger transitions). This feature is also recognized in figure 6(a) where the occupations of the lowest shown projectile levels increase for  $b < 18$ . The reason for no Auger emission at larger values of  $b$  is that we require at least two electrons in each shell for a fast Auger transition to become possible. With respect to the target (figure 6(b)), level  $m = 15$  is most active at all displayed impact parameters. Resonant loss into levels  $16 < m < 20$  occurs at the smallest shown impact parameters, but is comparatively small.

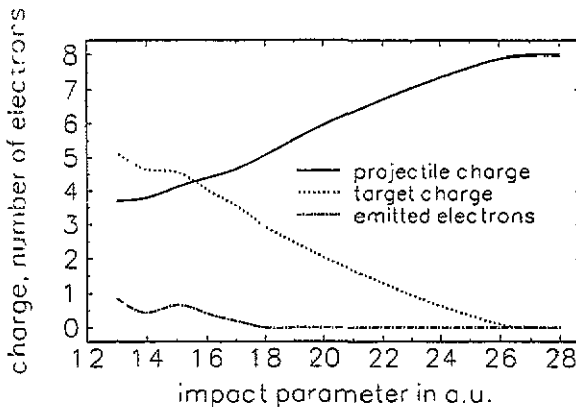
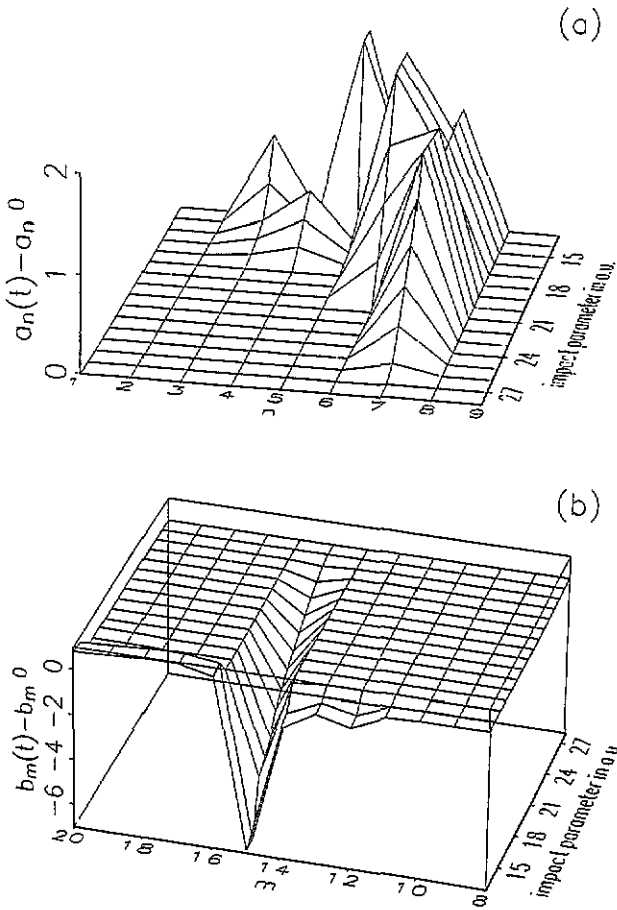


Figure 5. Final charge states and numbers of emitted Auger electrons for 80 keV  $\text{Ar}^{8+}$  ions colliding with  $\text{C}_{60}$  as a function of the impact parameter.

In the experiment of Walch *et al* (1994), final target charge states  $q^{(t)}(\infty)$  between 1+ and 6+ have been measured in coincidence with projectile ions in final charge states  $q^{(p)}(\infty) = 6$  and 7. According to this experiment, there is evidence that the  $\text{C}_{60}$  cage is destroyed in close collisions with impact parameters  $b < 14$ . By assuming a minimal impact parameter for non-destructive collisions of  $b_{\min} = 13$ , our simulation predicts a highest final target charge state of  $q^{(t)}(R_{\parallel} = 150) = q^{(t)}(\infty) \approx 5.2$  at  $b_{\min}$ . At larger impact parameters, smaller target charge states are predicted (figure 5). With respect to the final projectile charge-state distribution in collisions that preserve the carbon cage of  $\text{C}_{60}$ , our simulation predicts values of  $q^{(p)}(\infty)$  between about 4 and 8. We may assume, that down-stream Auger relaxation, due to slow Auger transitions, leads to the emission of two additional electrons before the projectile has reached a stable state. This assumption is supported by the results shown in figure 6(a) where, for impact parameters leading to  $q^{(p)}(\infty) = 4$  and 5 (cf figure 5), about four electrons are in highly-excited states. Even though these highly-excited states are relaxed with respect to fast Auger transitions, slow Auger transitions, with active electrons initially in different shells, result in the emission of about two more electrons. Including slow Auger transitions and with respect to charge-state changing collisions, our simulation therefore predicts final charge states between 1+ and 5+ for the target, and the final charge states 6+ and 7+ for the projectile, in agreement with the experimental results of Walch *et al* (1994).

The spectrum of emitted Auger electrons, resulting from fast Auger transitions, is displayed in figure 7 as a function of  $b$ . In addition to the two features observed in figure 4, a new structure appears between 12 and 34 eV for  $b < 15$ . According to figure 6(a), this



**Figure 6.** Final occupation changes of projectile levels  $n$  (a) and target levels  $m$  (b) as a function of the impact parameter. System and parameters as in figure 5.

structure is related to the dominant filling of projectile level  $n = 5$ , which occurs only at  $b < 15$ . Subsequent Auger decay increases the populations in levels  $n = 3$  and 4 (for  $b = 13$ ) and  $n = 3$  (for  $b = 14$ ). In figure 8 we show the Auger yield  $y_k$  differential in energy after integration over impact parameters between  $b_{\min}$  and  $R_1^*$

$$y_k = \frac{2\pi}{A} \int_{b_{\min}}^{R_1^*} db b c_k(b) \tag{13}$$

where  $c_k$  is the number of electrons collected in the  $k$ th energy bin, as shown in figure 7. We normalized  $y_k$  to the area  $A$  perpendicular to the incident beam direction that is run through by projectiles on charge-state changing trajectories

$$A = \pi(R_1^{*2} - b_{\min}^2). \tag{14}$$

### 6.3. Cross sections

In the experiment of Walch *et al* (1994) cross sections  $\sigma_i$  for the production of specific charge states  $+i$  of  $C_{60}$  have been measured. The critical distances  $R_i^*$  (10) for sequential

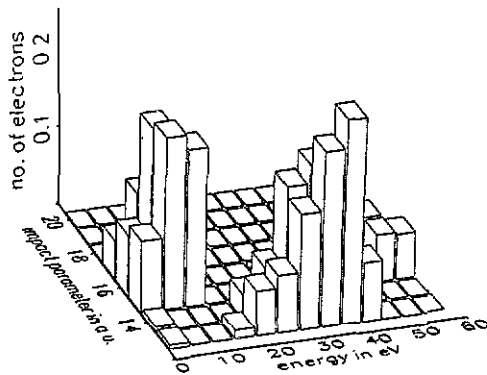


**Figure 7.** Projectile Auger-electron yield as a function of impact parameter and emitted electron energy. The energy bins have a width of 4.4 eV. System and parameters as in figures 5 and 6.

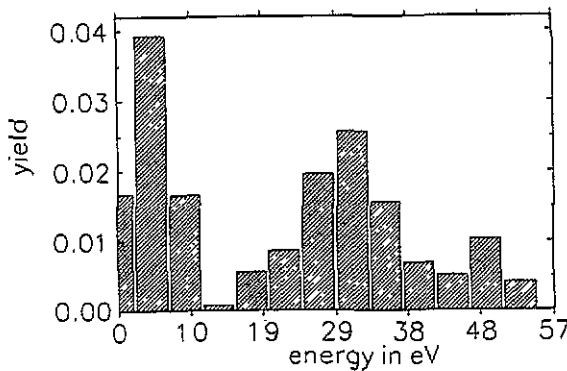


**Figure 8.** Projectile Auger-electron yield of figure 7, integrated over impact parameter and normalized according to equations (13) and (14).

over-barrier capture can be related to cross sections by

$$\sigma_i = \pi(R_i^{*2} - R_{i+1}^{*2}) \quad (15)$$

and to the total geometrical cross section for charge exchange in non-destructive collisions  $\sigma_{\text{tot}} = \pi R_1^{*2}$ .

Theoretical estimates for the critical over-barrier distances can be extracted from the impact-parameter-dependent final charge states of the target in figure 5. Table 3 shows a comparison of the experimentally determined radii  $R_{i,\text{exp}}^*$  with theoretical values  $R_{i,\text{theory}}^*$  from our simulation together with theoretical cross sections  $\sigma_{i,\text{theory}}$ , calculated according to (15). The theoretical value  $R_{1,\text{theory}}^*$  leads to  $\sigma_{\text{tot}} = 6.2 \times 10^{-14} \text{ cm}^2$ , which agrees well with the experimental result of  $(4.4 \pm 1.8) \times 10^{-14} \text{ cm}^2$ .

## 7. Summary and conclusions

We have formulated a theory for the simulation of charge transfer and electron emission in slow collisions between highly charged ions and spherical clusters. The theory is based on

Table 3. Theoretical ( $R_{i,\text{theory}}^*$ ) and experimental ( $R_{i,\text{exp}}^*$ ) critical over-barrier radii for electron capture in 80 keV Ar<sup>8+</sup> on C<sub>60</sub> collisions. The theoretical cross sections  $\sigma_{i,\text{theory}}$  for the production of final target charge states  $+i$  are related to  $R_{i,\text{theory}}^*$  by equation (15).

$i$	$R_{i,\text{exp}}^*$	$R_{i,\text{theory}}^*$	$\sigma_{i,\text{theory}} \times 10^{-15} \text{ cm}^2$
1	22.4±4.6	26.5	16
2	20.0	22.8	9.8
3	17.8	20.2	7.7
4	16.0	17.9	5.7
5	14.5	16.0	7.2
6	13.9	13.2	—

classical rate equations for the population dynamics of projectile and target levels and on estimates for resonant and Auger transition rates. The resonant transition rates are modelled on the basis of a classical over-barrier description of electron transfer in conjunction with hydrogenic projectile levels. Our simulation estimates the evolution of occupation numbers and projectile Auger electron emission in non-destructive collisions. It allows for the prediction of final charge states and energy-resolved Auger spectra.

In a first numerical application, we considered 80 keV Ar<sup>8+</sup> ions colliding with gaseous C<sub>60</sub>. Our results for the occupation dynamics of target and projectile levels illustrate the dynamical flow of electrons to and from particular levels. In view of only one adjustable parameter ( $b_{\text{min}}$ ) in the scattering part of our calculation, the predicted final charge-state distribution of target and projectile, the cross section for the production of particular target charge states and the total cross section for non-destructive charge-state changing collisions agree well with recent experimental data. We plan to further refine our simulation by including the radiative relaxation of multiply excited projectiles and slow Auger relaxation channels. We hope that more experimental data, including energy-resolved emitted electron spectra and scattering angle-differential charge-state distributions, will soon become available and facilitate refinement and tests of our simulation.

## Acknowledgments

I am grateful to C L Cocke and B Walch for stimulating discussions. This work was supported by the Division of Chemical Sciences, Basis Energy Sciences, Office of Energy Research, US Department of Energy.

## References

- Benning P J, Poirier D M, Troullier N, Martins J L, Weaver J H, Haufier R E, Chibante L P F and Smalley R E 1991 *Phys. Rev. B* **44** 1962
- Burgdörfer J, Lerner P and Meyer F W 1991 *Phys. Rev. A* **44** 5674
- Cowan R D 1981 *The Theory of Atomic Structure and Spectra* (Berkeley: University of California Press)
- Jost M B, Troullier N, Poirier D M, Martins J L, Weaver J H, Chibante L P F and Smalley R E 1991 *Phys. Rev. B* **44** 1966
- Krätschmer W, Lamb L D, Fostiropoulos K and Huffman D R 1990 *Nature* **347** 354
- Kroto H W, Allaf A W and Balm S P 1991 *Chem. Rev.* **91** 1213 and references therein
- Kroto H W, Heath J R, O'Brian S C, Curl R F and Smalley R E 1985 *Nature* **318** 162
- Jackson J D 1975 *Classical Electrodynamics* (New York: Wiley)
- Jones D E H 1966 *New Scientist* **32** 245

- Martins J L, Troullier N and Weaver J H 1991 *Chem. Phys. Lett.* **180** 457
- Osawa E 1970 *Kagaku* **25** 854 (in Japanese)
- 1991 *Chem. Abstr.* **74** 75 698v
- Puska M J and Nieminen R M 1993 *Phys. Rev. A* **47** 1181 and references therein
- 1994 Private communication
- Saito S and Oshiyama A 1991 *Phys. Rev. Lett.* **66** 2637
- Satpathy S 1986 *Chem. Phys. Lett.* **130** 545
- Smith F T 1961 *J. Chem. Phys.* **34** 793
- Walch B, Cocke C L, Voelpel R and Salzborn E 1994 *Phys. Rev. Lett.* **72** 1439
- Wang S, Trajmar S and Khakoo M A 1983 *J. Phys. B: At. Mol. Phys.* **26** 3639 and references therein.
- Weaver J H, Martins J L, Komeda T, Chen Y, Ohno T R, Kroll G H, Troullier N, Hauffler R E and Smalley R E  
1991 *Phys. Rev. Lett.* **66** 1741